Research Square

Preprints are preliminary reports that have not undergone peer review.
They should not be considered conclusive, used to inform clinical practice,
or referenced by the media as validated information.

Polydopamine Surface Engineering of Iron Single-Atom Nanozyme: a Novel Strategy for Doxorubicin Immobilization, Tumor Microenvironment Remodeling and Synergistic Multimodel Therapy

Meiling Liu

liuml@hunnu.edu.cn

Hunan Normal University

Jing Liu

Hunan Normal University

Minjuan Wang

School of Pharmacy, Xianning Medical College, Hubei University of Science and Technology

Haoyu Chen

Hunan Normal University

Xing Yang

Hunan Normal University

Mingjie Wei

School of Pharmacy, Xianning Medical College, Hubei University of Science and Technology

Xingfeng Wang

Hubei University of Science and Technology

Shigang Shan

Hubei University of Science and Technology

Xiaohua Zhu

Hunan Normal University

Youyu Zhang

Hunan Normal University

Shouzhuo Yao

Hunan Normal University

Article

Keywords: Single-Atom Nanozymes, Multi-Mimics, Polydopamine, Photothermal, Synergistic Therapy

Posted Date: May 21st, 2024

DOI: https://doi.org/10.21203/rs.3.rs-4413121/v1

License: This work is licensed under a Creative Commons Attribution 4.0 International License.
Read Full License

Additional Declarations: There is **NO** Competing Interest.

Abstract

The variation in tumor microenvironment, specifically the levels of cellular H_2O_2/O_2/GSH, plays a crucial role in the effectiveness of cancer therapy in nanozyme-drug systems. In this study, bioinspired polydopamine was utilized to surface engineer the rhombic dodecahedron morphology iron-based SANzyme (Fe SANzyme), which exhibited multiple mimetic activities including oxidase (OXD)-like, peroxidase (POD)-like, catalase (CAT)-like, and glutathione peroxidase (GPx)-like activities. The Fe SAN-PDA was intricately designed as a nanoplatform for drug immobilization, remodeling the tumor microenvironment (TME) and enabling synergistic multimodal tumor therapy. The presence of abundant quinone structures on PDA surface facilitated the creation of a conductive microenvironment for the immobilization of doxorubicin (DOX) through Michael addition/Schiff base reaction. The Fe SAN-PDA@DOX can catalyze high level of H_2O_2 in TME to produce oxygen and alleviate hypoxia, convert the produced oxygen to the toxic ·OH, and deplete intracellular glutathione. Coating with hyaluronic acid (HA) enhanced the biocompatibility and targeting ability of the composite. The exceptional photothermal performance of Fe SAN-PDA@DOX@HA, combined with the nanozyme catalysis, resulted in sustained chemodynamic/photothermal/ chemotherapy is achieved in a mouse mammary carcinoma model. This research highlights the synergistic therapeutic effects resulting from the combination of the multi-enzymatic activities of Fe SAN with multifunctional PDA, offering a novel a novel strategy for doxorubicin immobilization, tumor microenvironment remodeling and synergistic multimodal therapy.

Introduction

A new generation of artificial enzymes, nanozymes, based on nanotechnology and nanomaterials, have emerged with intrinsic enzyme-mimicking catalytic ability[1]. These nanozymes offer advantages such as higher stability[2], outstanding catalytic activity, lower manufacturing cost[3], and ease of modification. As a result, nanozyme-mediated approaches have been widely explored as a weapon to inhibit tumor cell proliferation[4], including chemodynamic therapy (CDT), phototherapy (PTT), photodynamic therapy (PDT), sonodynamic therapy (SDT), chemotherapy (CT), radiotherapy (RT) and immunotherapy[5]. In the past decade, there has been significant advancement in the field of nanozyme[6], with the discovery of various types such as noble metal nanomaterials, metal oxides, two-dimensional nanosheets and carbon-based nanomaterials, all exhibiting diverse enzyme-like functions. These functions encompass oxidase (OXD)-like[7], peroxidase (POD)-like[8], catalase (CAT)-like[9], superoxide dismutase (SOD)-like[10], glutathione peroxidase (GPx)-like[11], and hydrolase-like activities[12], which hold the potential to impact intracellular oxidative homeostasis and induce cell death. Within the mild acidic and high level of hydrogen peroxide (H_2O_2) of the tumor microenvironment (TME), nanozymes are specifically designed to trigger enzymatic chemical reactions, generating a significant amount of toxic reactive oxygen species (ROS) to eliminate tumor cells, thus representing a promising antitumor approach[13]. Notable examples include PEGylated $Cu_xMn_yS_z$ (PCMS) with OXD-like activity converting oxygen into superoxide radicals $\cdot O_2^-$ in TME[14] and PtMo-Au metalloenzyme with POD-like activity inducing oxidative stress to trigger cell apoptosis for

cascade CDT[15]. These advancements offer potential opportunities to leverage the catalytic activities of nanozymes to disrupt delicate homeostasis and enhance the synergistic treatment effects in the domain of cancer-specific therapies. However, the presence of hypoxia in the TME of many solid tumors poses a challenge[16], as it enhances resistance to chemotherapy and diminishes the effectiveness of chemotherapeutic drugs. Nanozymes with CAT mimic capabilities have shown promise in improving the efficiency of radiotherapy and photodynamic therapy by addressing tumor hypoxia. While these approaches have been shown promise in enhancing the efficacy of PDT or CT, the oxygen-dependent therapies may closely linked to the complexities of the chemotherapy and the therapeutic effect of drugs. As such, the development of a multifunctional nanozyme shows great promise. Further exploration in this direction could lead to significant advancements in cancer treatment strategies.

Single atom nanozymes (SANzymes) have recently garnered considerable attention in the realm of catalytic therapy of tumors, owing to their unique characteristics, such as maximum atomic utilization, distinctive electronic structure, and highly exposed catalytic active sites[17–18]. Their capability to respond to specific endogenous physiological environments by activating catalytic sites and facilitating irreversible oxidative damage reactions has piqued interest within the scientific community. With the rapid advancements in nanomedicine, the impressive catalytic activity, ease of modification, and functional richness of SANzymes present a myriad of opportunities for broader applications. In the context of tumor treatment, SANzymes exhibit multi-mimics properties, enabling the production of various ROS[19] such as singlet oxygen ($^1O_2$), superoxide radicals ($O_2{\cdot}^-$), hydroxyl radicals (·OH), and peroxides (O_2^{2-}), thus laying the groundwork for potential nano-cooperative diagnosis and treatment based on ROS catalysis. For instance, Cu-SANzyme, boasting exceptional CAT-like activity, can mitigate hypoxia in tumor cells, leading to cell apoptosis or necrosis[20]; While iridium (Ir) SAzyme has demonstrated remarkable POD-like activity, converting excess H_2O_2 into highly toxic ·OH[21]. The diverse mimics of SANzyme in tumor therapy hold significant promise. Nevertheless, the current focus of SANzyme-based catalysis for therapy predominantly revolves around catalysis therapy, often resulting in limited therapy efficacy. For example, Liu and colleagues designed a single-atom nanoagent with POD-like activity, effectively initiating an in-situ tumor-specific Fenton reaction to selectively generate ·OH in the acidic TME for CDT[22]. The development of single atom copper (Cu)-doped hollow TiO_2 nanosonosensitizers for synergistically enhanced sonodynamic and chemodynamic nanotherapies against triple-negative breast cancer represents a significant advancement in cancer treatment[23]. While existing research has primarily focused on harnessing the POD mimic properties in therapy, a notable lack of attention towards leveraging the multi-enzyme properties simultaneously and overlooking the potential to regulate and remodel the TME. Combing single atom nanozymes with drugs has shown promise in achieving synergistic therapy, as evidenced by the cobalt-single-atom nanozyme when combined with doxorubicin (DOX) [24]. However, the efficacy of current anti-tumor drugs is limited by their weak anti-tumor effect and poor accumulation at the tumor site, leading to potential damage to hematopoietic stem cells and renal toxicity[25]. Therefore, developing a strategy to chemically immobilize anticancer drugs on the surface of single-atom nanozymes presents a valuable opportunity. This

approach not only enables controlled drug release within the TME but also facilitates TME remodeling and multi-mode therapy. The integrating additional therapeutic modalities such as PTT, CT, and PDT, while leveraging the ROS-regulating capabilities of SANzymes, it is possible to mitigate tumor drug resistance and enhance the efficacy of cancer treatment.

The bioinspired concept derived from polydopamine (PDA), a mussel-inspired polymer renowned for its versatile surface coverage capabilities, has emerged as a valuable material in both chemical and biomedical domains[26]. The presence of abundant polyphenol groups on the surface of PDA facilitates chemical reactions, establishing a conducive microenvironment for further modification, drugs loading and controlled release within the TME. Moreover, PDA-based nanomaterials exhibit favorable biocompatibility. This innovative strategy of loading doxorubicin (DOX) onto PDA-functionalized SANzymes presents a promising avenue to circumvent the direct impact of DOX on healthy organs, potentially enabling synergistic multi-mode therapies. At the same time, PDA's responsiveness to the TME, coupled with its slow degradation profile, supports the controlled release of DOX, enhancing drug retention and utilization while harnessing its superior photothermal properties for enhanced cancer treatment outcomes. Consequently, by leveraging bioinspired polydopamine for surface engineering of single-atom nanoenzymes, the combined structural and functional benefits of PDA, alongside the diverse mimics of single-atom nanozymes can be fully harnessed, offering significant potential in TME reshaping, efficient drug loading and releasing, and multimodal tumor treatment strategies.

In this study, a novel strategy for immobilizing doxorubicin, remodeling tumor microenvironment, and conducting synergistic multimodal therapy was proposed. The bioinspired polydopamine was used to surface engineer the rhombic dodecahedron morphology iron-based SANzyme (Fe SANzyme), resulting in the production of Fe SAN-PDA. This composite displayed multiple mimetic activities, such as oxidase (OXD)-like, peroxidase (POD)-like, catalase (CAT)-like, and glutathione peroxidase (GPx)-like activities. Through the incorporation of polyphenol and quinone structures on the PDA surface, doxorubicin with amino groups could be intricately immobilized on Fe SAN-PDA via Michael addition/Schiff base reaction under weak alkaline conditions. The nanocomposites were able to catalytically decompose endogenous H_2O_2 into O_2, alleviate hypoxia, and generate cytotoxic hydroxyl radical (·OH) in TME, but also effectively consume intracellular GSH to enhance local oxidative stress in tumor cells. Additionally, the composite exhibited significant photothermal performance under 808 nm laser irradiation, enhancing the antitumor efficacy of catalytic therapy. Further modification with hyaluronic acid (HA) improved the targeting ability, biocompatibility and bio-distribution of the composite in vivo. As illustrated in Scheme 1, this multifunctional nanocomposite not effectively regulated the redox balance within cells, induces apoptosis of cancer cells, and demonstrated anti-tumor effects in a mammary carcinoma model, showcasing the potential of synergistic CDT/PTT/CT therapy. This research presents a novel strategy for surface engineering Fe SAN with PDA for doxorubicin immobilization, highlighting the multifunctionality of PDA diverse capabilities of Fe SAN-PDA for H_2O_2/O_2/GSH regulation, tumor microenvironment remodeling, and synergistic multimodal therapy.

Results

Synthesis and Characterization of Fe SAN-PDA@DOX@HA.

The fabrication and synthesis approach for the Fe SAN-PDA@DOX@HA nanoplatform is detailed in Scheme 1. First, the iron single atom nanozyme (Fe SAN) was successfully produced by synthesizing Fe@ZIF-8 as a precursor under N_2 atmosphere through high temperature annealing at 900°C for 3 h. The TEM and SEM images in **Fig. 1a** and **Figures S1-S2** show the regular polyhedral morphology of Fe SAN with uniform dimensions of approximately 150 nm in diameter. High resolution TEM (HR-TEM) images and selected area electron diffraction (SAED) results confirm the amorphous nature of Fe SAN, devoid of Fe nanoparticles as evidenced in **Figure S3** and **S4**. The high-angle annular dark-field scanning transmission electron microscopy (HAADF-STEM) image, after differential phase contrast correction, reveals the scattering of individual Fe atoms denoted by bright spots encircled in red **(Fig. 1c and 1d)**. Dopamine undergoes oxidation and self-polymerization under weak alkaline conditions, leading to the formation of PDA that envelops the surface of Fe SAN. The presence of a PDA layer surrounding Fe SAN, increasing the thickness of the material to about 200 nm, is evident in **Fig. 1b** and **Figure S5 and S6**. Energy dispersive X-ray spectroscopy (EDS) mapping **(Fig. 1e)** further validates even distribution of Fe, C and N elements within Fe SAN.

The powder X-ray diffraction (XRD) spectra of Fe SAN and Fe SAN-PDA exhibit two prominent peaks at 24° and 43°, corresponding to the (002) and (100) planes of carbon **(Fig. 1f)**, indicating the amorphous nature of Fe SAN-PDA, consistent with the TEM and HR-TEM results. The structural similarity between Fe SAN and Fe SAN-PDA post PDA coating is evident, as supported by XPS spectra in **Fig. 1g** showing distinct peaks for C, O, and N in both materials[27–28]. While the iron peak pronounced in both cases, possibly due to the relatively low iron content. The N1s fitting peaks in Fe SAN display peaks at 398.03 and 399.5 eV, assigned to pyridinic and pyrrolic N, respectively. Conversely, the N1s fitting peaks of Fe SAN-PDA consist of peaks at 399.4, 400.2, and 401.1 eV, corresponding to C = N-R, R_1-NH-R_2, and R-NH_2 structures **(Fig. 1h)**, respectively, indicating a change in the valence state of N atoms after PDA encapsulation. The high-resolution Fe 2p XPS spectrum of Fe SAN **(Figure S7)** shows two peaks assigned to Fe $2p_{3/2}$ (715.6 eV) and Fe $2p_{1/2}$ (726.7 eV). The split peaks of C1s at 284.6, 285.2, and 286.0 eV correspond to C-H, C-O, and C = O of carbon atoms **(Figure S8)**. The O1s peaks including -OH, C = O, and C-O are located at 531.8, 532.7, and 533.7 eV, while the C = O peak results from the oxidation of catechol groups in dopamine to quinones **(Figure S9)** [29]. The XPS spectra results show similar elemental composition before and after PDA coating. The elemental compositions and contents of Fe SAN and Fe SAN-PDA nanomaterials are shown in **Table S1**. The elemental contents indicate a decrease in Fe content and a significant increase in O content after PDA modification, probably due to the abundant phenolic hydroxyl groups on the PDA surface. FTIR and UV spectra further confirm the successful modification of PDA[30]. The IR spectrum shows that after PDA modification, the peak at 1299 cm^{-1} appeared due to the stretching vibration of = C-H. The peaks at 1384 and 1610 cm^{-1} are attributed to the bending vibration of amino groups (N-H) in the benzene ring and the stretching vibration of C = C, while

the peak at 3425 cm^{-1} corresponds to the N-H stretching vibration **(Fig. 1i)**. These detailed characterizations underscore the successful synthesis of Fe SAN-PDA, with the outer PDA layer potentially enhancing photothermal performance and facilitating drug loading capabilities[31].

Investigating the local atomic electronic structure and coordination environment of Fe atoms in Fe SAN involved conducting synchrotron radiation-based X-ray absorption near-edge structure (XANES) and extended X-ray absorption fine structure (EXAFS) measurements. The Fe K-edge XANES spectra **(**Fig. 2a**)** indicated that the energy absorption threshold of Fe SAN falls between Fe foil and Fe_2O_3, suggesting the presence of positively charged $Fe^{\delta+}$ stabilized by N atoms within Fe SAN[32]. Analysis of the Fourier-transformed (FT) κ^3-weighted EXAFS spectrum revealed a predominant peak at about 1.50 Å, corresponding to the Fe-N scattering path, indicating the absence of Fe clusters or particles and the atomic dispersion of Fe species in SAzymes **(**Fig. 2b**).** Further EXAFS fitting **(**Fig. 2c and S10 **and Supporting Information Table S2)** confirmed that each Fe atom was coordinated by an average of four N atoms, with an average Fe-N bond length of 1.99 Å, indicating a four-coordinated structure of Fe sites with nitrogen species. The wavelet transform (WT) contour plot of the Fe k-edge EXAFS oscillations supported the atomic dispersion of Fe throughout the Fe SAN, with a single intensity maximum at 5 $Å^{-1}$ attributed to Fe-N bonding **(**Fig. 2d-f**)**. The absence of an intensity maximum corresponding to Fe-Fe bonding in the WT plots further reinforced the presence of atomic dispersion of Fe atoms on the C-N support, as demonstrated by both FT- and WT-EXAFS analyses.

Tetra-enzyme Mimic Activities of Fe SAN-PDA Nanoparticles.

The multi-mimetic properties of Fe SAN-PDA were first investigated, focusing on its POD- and OXD-like activities using 3,3',5,5'-tetramethylbenzidine (TMB) as a chromogenic substrate, as depicted in Fig. 3a. The introduction of H_2O_2 and Fe SAN-PDA resulted in the emergence of a distinct absorption peak of oxidized TMB at 652 nm **(**Fig. 3b**)**, indicating the favorable POD-like characteristics of Fe SAN-PDA. Moreover, the intensity of the absorption peak of the ox-TMB at 652 nm exhibited a concentration-dependent relationship with Fe SAN-PDA, gradually rising with increasing Fe SAN-PDA concentration, as demonstrated in Fig. 3c. The impact of varying pH levels on the POD-like activity of Fe SAN-PDA was also investigated, revealing a stronger absorbance peak of ox-TMB at pH 5.5 compared to pH 7.4 **(**Fig. 3d**)**. In addition, the absorbance of ox-TMB at 652 nm increased over time **(Figure S11)**. Using Michaelis-Menten reaction kinetics offered a thorough assessment of the POD-like activity of Fe SAN-PDA, with linear regression equations derived for different TMB and H_2O_2 concentrations as $y = 0.227x + 0.249$ ($R^2 = 0.992$, K_m and V_{max} were 0.9 mM and 4.01×10^{-7} M s^{-1}) and $y = 6.35x + 1.03$ ($R^2 = 0.996$, K_m and V_{max} values of 0.62 mM and 0.97×10^{-7} M s^{-1}), respectively **(**Fig. 3e-3h**)**. The lower K_m value compared to other nanozymes **(Table S3)**, indicates the strong affinity of Fe SAN-PDA for TMB and H_2O_2. Moreover, the higher V_{max} suggests the POD-like catalytic activity of Fe SAN-PDA nanocomposites. This remarkable activity can be attributed to the high content of pyridinic N content in Fe SANs, which supports the adsorption of H_2O_2. H_2O_2 binds geometrically to Fe atoms, triggering the activation of H_2O_2

($^{*}H_2O_2$), which leads to the cleavage of the O-O bond in $^{*}H_2O_2$ to produce two activated OH ($^{*}OH$). Subsequently, one $^{*}OH$ separates from the Fe site to form ·OH. The reaction mechanism elucidates the exceptional POD-like catalytic behavior of Fe-SAN, highlighting its potential for a wide range of applications.

In order to further substantiate the catalytic mechanism of the POD-like activity and and ascertain whether Fe SAN-PDA facilitates the production of the active species ·OH from H_2O_2„ validation experiments were conducted utilizing methylene blue (MB) for confirmation purposes. MB, a widely used blue organic dye, undergoes degradation to a colorless form in the presence of ·OH, rendering it suitable for confirming the generation of ·OH **(**Fig. 3i**)**. The results depicted in **Figure S12** reveal a notable reduction in the characteristic absorption peak of MB at 660 nm when Fe SAN-PDA and MB were combined with H_2O_2 and allowed to react for 30 min, with the absorbance of MB progressively declining over time **(**Fig. 3j**)**. Moreover, the utilization of coumarin as a trap led to the production offluorescent 7-hydroxycoumarin, further corroborating the generation of ·OH **(Figure S13a)**. Upon mixing Fe SAN-PDA and coumarin solution with H_2O_2, a gradual increase in the fluorescence peak intensity of 7-hydroxycoumarin at 457 nm was observed **(Figure S13b)**. These findings underscore the effective catalysis of·OH formation from H_2O_2 by Fe SAN-PDA, thereby facilitating the oxidation of TMB to ox-TMB. The generation of ·OH under mildly acidic conditions (pH 5.5) presents a promising strategy for efficiently generate ROS within cells, thereby establishing conducive conditions for CDT.

The investigation into the OXD-like activity and kinetics of Fe SAN-PDA was extended to explore its potential oxygen consumption. In the Fe SAN-PDA + TMB group at pH 4.0, a distinct absorption peak at 652 nm emerged, signifying the OXD-like activity of Fe SAN-PDA **(**Fig. 3k**)**. Through manipulation of the TMB concentration **(**Fig. 3l**)**, a typical Michaelis-Menten plot for the OXD mimic of Fe SAN-PDA was obtained **(Figure S14)**, yielding a linear regression equation of y = 0.227x + 0.466 (R^2 = 0.988). The calculated K_m and V_{max} values for TMB were 0.215 mM and 4.88×10^{-7} M s^{-1}, respectively. The relatively high V_{max} of Fe SAN-PDA in comparison to other OXD-like nanocatalysts **(Table S3)** suggests commendable satisfactory catalytic efficiency, while the K_m value indicates a moderate affinity for TMB **(Table S3)**. Nevertheless, it was observed that under weakly acidic to nearly neutral conditions, the OXD-like activity of Fe SAN-PDA was found to be almost negligible at pH 5.5 and 6.5 **(Figure S15)**.

The CAT-like activity of Fe SAN-PDA nanomaterials in catalyzing the conversion of H_2O_2 to O_2 was further investigated. The O_2 production was assessed by monitoring the decline in fluorescence (E_x 455 nm) of the typical O_2 probe, $[Ru(dpp)_3]Cl_2$ (RDPP). The CAT-like behavior of Fe SAN-PDA was evaluated by quantifying the O_2 generated upon the introduction of Fe SAN-PDA nanocomposites into the H_2O_2 solution. Upon the addition of H_2O_2 and Fe SAN-PDA, the fluorescence of RDPP decreased **(**Fig. 4a**)**, indicating O_2 production. The presence of Fe SAN-PDA led to a notable decrease in RDPP fluorescence over time, achieving a quenching efficiency of 50% within 15 mins, as shown in **Figure S16**. The study observed a slight in fluorescence quenching of RDPP with higher pH values **(Figure S17)**. Compared to

the control group, Fe SAN-PDA nanocomposites efficiently generated a substantial amount of oxygen (Fig. 4b and **Figure S18)**. Moreover, the oxygen production by catalytic action of Fe SAN-PDA in PBS at varying pH values was quantified using a dissolved oxygen meter, yielding consistent results (Fig. 4c). The catalytic kinetics analysis of Fe SAN-PDA through the Michaelis-Menten reaction unveiled a K_m of 0.0113 mM and V_{max} of 5.85×10^{-6} M s^{-1} for H_2O_2 **(Figures S19)**, demonstrating its promising CAT-like activity. Notably, even at pH 6.5, Fe SAN-PDA displayed the ability to produce a significant quantity of oxygen, indicating its potential of Fe SAN-PDA to mitigate tumor cell hypoxia under mildly acidic conditions, thus presenting encouraging prospects for cancer treatment.

The utilization of titanium sulfate ($Ti(SO_4)_2$) probe has facilitated the confirmation of Fe SAN-PDA in the consumption of H_2O_2 and the production of O_2. This phenomenon was ascribed to the reaction between H_2O_2 and $Ti(SO_4)_2$, leading to the generation of a yellow precipitate of peroxo-titanium complex. The assessment of H_2O_2 consumption was carried out through colorimetric analysis of absorbance at 415 nm. As illustrated in **Figure S20**, the introduction of Fe SAN-PDA into the H_2O_2 system resulted in a notable reduction in intensity of absorbance peak at 415 nm. With time, the absorbance at 415 nm progressively decreased (Fig. 4d). These findings indicate that Fe SAN-PDA effectively expedited the decomposition of H_2O_2 into oxygen, demonstrating its ability to alleviate hypoxia in the TME. Consequently, the marginal OXD-like activity minimally impacts the oxygen generated by the CAT-like function of Fe SAN-PDA, thereby preserving the catalytic efficacy of the CAT mimic.

In the TME, the presence of GSH at concentrations ranging from 1–10 mM has been noted to counteract the ROS produced by the nanomaterial catalysis, potentially impacting the therapeutic effectiveness of the process. To address this issue, an examination of the GPx-like activity of Fe SAN-PDA was conducted. The confirmation of GPx-like activity in Fe SAN-PDA nanocomposites was established through experiments involving the simultaneous presence of GSH and H_2O_2, in conjunction with the addition of glutathione reductase (GR) and nicotinamide adenine dinucleotide phosphate (NADPH). The conversion of GSH to GSSG in the presence of H_2O_2, followed by regeneration to GSH by GR in the presence of NADPH, was observed. In particular, the characteristic UV-visible absorption peak of NADPH at 340 nm was utilized to evaluate the GPx-like activity of Fe SAN-PDA. The results, depicted in **Figure S21**, illustrated that the introduction of Fe SAN-PDA expedited the conversion of GSH to GSSG and the subsequent reduction of NADPH to $NADP^+$, as indicated by a notable decrease in the peak at 340 nm. These findings unequivocally validated the impressive GPx-like catalytic performance of Fe SAN-PDA. Furthermore, the GSH-depleting capacity of Fe SAN-PDA was assessed using 5,5'-dithiobis-(2-nitrobenzoic acid) (DTNB), a GSH indicator. The reaction of GSH with DTNB led to the generation of yellow products with a distinct absorbance at 412 nm (Fig. 4e). Over various time intervals, the GSH concentration gradually diminished in the presence of Fe SAN-PDA (Fig. 4f and 4g). These results highlighted the GPx-like activity of Fe SAN-PDA, which efficiently consumed GSH, thereby alleviating the impact of elevated GSH levels on ·OH consumption and ultimately contributing to enhanced efficiency in anti-tumor therapy.

The results presented above highlight the diverse catalytic capabilities of Fe SAN-PDA in vitro (Fig. 4h). In the TME, the CAT mimic efficiently converts endogenous H_2O_2 into oxygen, playing a crucial role in alleviating hypoxia. Furthermore, the POD mimic facilitates the generation of highly toxic ·OH from H_2O_2 and triggers the oxidation of GSH to GSSG through GPx-like activity, thereby intensifying oxidative stress in tumor cells. This multi-nanozyme functionality of Fe SAN-PDA holds great promise in modulating the intracellular levels of key molecules like GSH, O_2, and H_2O_2, thereby enabling precise regulation of cellular processes through nanozyme-mediated catalysis. These findings open up exciting avenues for catalytic-based diagnosis and therapeutic strategies, which warrant further comprehensive exploration.

Photothermal Properties of Fe SAN-PDA Nanoparticles.

PDA stands out as an outstanding photothermal material that significantly boosts photothermal efficiency owing to its wide light absorption characteristics spanning the visible to near-infrared spectrum. The absorption of near-infrared light plays a crucial role in photothermal therapy (PTT). Aqueous dispersions of Fe SAN-PDA at various concentrations underwent irradiation with an 808 nm laser for 6 minutes, while time-resolved thermal imaging tracked temperature alterations. The findings revealed that exposure to a 1.2 W cm^{-2} of 808 nm laser elevated the temperature of the Fe SAN-PDA (200 μg·mL^{-1}) solution from 26.5°C to 61.0°C. Noteworthy is the the gradual temperature rise with increasing concentration of Fe SAN-PDA, as illustrated in Fig. 4i. This temperature escalation proved adequate for cancer cell destruction through hyperthermia. Furthermore, the photothermal stability and sensitivity were confirmed by monitoring the temperature changes over five repeated “on/off” cycles at 808 nm (Fig. 4j). Fe SAN-PDA exhibited impressive photothermal characteristics, boasting a photothermal conversion efficiency of approximately 53.4% (Fig. 4k). Thermal imaging results for the respective concentrations align consistently, as depicted in Fig. 4l, corroborating the data in Fig. 4i. These outcomes underscore the commendable photothermal conversion capabilities of Fe SAN-PDA, signaling its potential as an effective PTT agent. Consequently, Fe SAN-PDA holds significant promise as a near-infrared photothermal nanomaterial and can be further utilized for subsequent synergetic photothermal therapy applications.

Drug-Loading and Release of Fe SAN-PDA@DOX@HA nanocomposite.

The biocompatible PDA surface, characterized by its abundance of phenolic hydroxyl and quinone structure, serves as a substrate for the conjugation of of doxorubicin (DOX) molecules. By employing the Michael addition/Schiff reaction, DOX can be effectively linked to the Fe SAN-PDA surface, leading to the formation of Fe SAN-PDA@DOX nanocomposite. The successful incorporation of DOX is evident from the emergence of a distinct absorption peak at around 480 nm in the UV spectrum of the resultant Fe SAN-PDA@DOX (Fig. 5a). Furthermore, the strong fluorescence signal at 590 nm (E_x 490 nm) observed in the fluorescence spectrum of DOX-loaded Fe SAN-PDA (Fig. 5b) confirms the presence of DOX. Further validation through infrared characterization reveals changes such as C-O at 1291 cm^{-1} and the broadening C = O stretching vibration band at 1691 cm^{-1} in the FTIR spectrum of Fe SAN-PDA@DOX

(Fig. 5c). These alterations signify the occurrence of the Michael addition reaction between the -NH_2 group on the DOX molecule and the quinone structure on the PDA, thereby affirming the successful modification of DOX on the PDA surface[33]. DLS analysis indicates that the diameter of Fe SAN measures is 255 nm. After PDA coating, the hydrated particle size increases significantly, reaching 615 nm. Moreover, the introduction of DOX onto the Fe SAN-PDA surface results in a slight additional augmentation in the hydrated particle size, as depicted in Fig. 5d. The zeta potential experiment demonstrates a notable shift in the potential value for Fe SAN-PDA@DOX in comparison to Fe SAN-PDA, signifying the effective coupling of DOX to the surface of Fe SAN-PDA (Fig. 5e).

The decrease in absorption peak of the supernatant at 480 nm following the introduction of Fe SAN-PDA suggests a modification of DOX onto the Fe SAN-PDA surface (Fig. 5f). The standard curve of DOX (Fig. 5g and 5h), was established by analyzing various standard DOX solutions. By correlating the UV absorbance value at 480 nm in Fig. 5f with the standard curve in Fig. 5h, the loading efficiency of DOX can be determined. The loading capacity (LC%) calculated to be 50.96% using the formula provided in Eq. 5 **in the Supporting Information**.

The investigation into the release behavior of DOX in PBS at different pH levels (5.5, 6.5, and 7.4) through UV-vis spectra analysis (Fig. 5i) revealed a notable pH-dependent impact on the in vitro release of DOX. Particularly at pH 5.5, the release rate of DOX peaked at 46.5%, underscoring the significant influence of weakly acidic conditions on release kinetics. This effect is attributed to the disruption of the C = N double bond between DOX and PDA, leading to accelerated DOX release. These observations lay the groundwork for the acid-responsive release of DOX in the TME. The successful loading and controlled release of DOX pave the way for future investigations into synergistic therapy potential of Fe SAN-PDA@DOX@HA in nanocatalysis and chemo/photothermal therapy.

In Vitro Cellular Uptake

The assessment of in vitro anti-tumor therapy targeting liver cancer cells (HepG2) commenced with the remarkable attributes of Fe SAN-PDA@DOX. To improve biocompatibility, extend blood circulation duration, and improve active targeting, a modification involving hyaluronic acid (HA) on the surface of Fe SAN-PDA@DOX was undertaken, resulting in the creation of Fe SAN-PDA@DOX@HA complex. The cytotoxicity impact of Fe SAN-PDA@DOX@HA on HepG2 cells and human normal liver cells (LO2) was initially evaluated by methylthiazolyl tetrazolium (MTT) assay. Findings illustrated in Fig. 6a and S22 demonstrated varying degrees of cytotoxicity across the different groups. Noteworthy was the progressive decline in survival rates with escalating concentration of Fe SAN-PDA@DOX@HA, indicating heightened cytotoxicity in contrast to Fe SAN-PDA@HA without DOX loading. Furthermore, the group treated with Fe SAN-PDA@DOX@HA + 808 nm exhibited elevated cytotoxicity, suggesting that the combined application of laser treatment with Fe SAN-PDA@DOX@HA can synergistically trigger photothermal and chemotherapy responses, thereby impeding cancer cell proliferation.

Endocytosis serves as the primary mechanism through which cells internalize nanomaterials. To investigate the cellular uptake behavior of Fe SAN-PDA@DOX@HA, we employed confocal laser scanning microscopy (CLSM) and flow cytometry techniques to assess the fluorescence intensity of DOX. The time-dependent increase in red fluorescence intensity of Fe SAN-PDA@DOX@HA within HepG2 cells demonstrated its efficient uptake, with significant fluorescence detected as early as 6 hours of incubation (Fig. 6b and S23). These findings, flow cytometry analysis (Fig. 6c) further substantiated the successful internalization of Fe SAN-PDA@DOX@HA. These outcomes not only validate the effective cellular uptake of the compound but also lay a solid foundation for future explorations in therapeutic applications.

Relieve hypoxia, intracellular reactive molecules regulation, and cytotoxicity of Fe SAN-PDA@DOX@HA

Higher oxygen levels have the capacity to extinguish the fluorescence of the oxygen probe $[Ru(dpp)_3]Cl_2$ (RDPP). Through an examination of the fluorescence of RDPP in conjunction with nanomaterials and cells utilizing CLSM, we can assess the catalytic oxygen generation of Fe SAN-PDA@HA within the cells. To minimize the interference stemming from the red fluorescence of DOX, our focus was directed towards monitoring alterations in intracellular O_2 catalyzed by Fe SAN-PDA@HA under 808 nm laser exposure, as shown in Fig. 6d and 6e. In comparison to the control group, the red fluorescence signal of the Fe SAN-PDA@HA + 808 nm group exhibited a notable decrease, indicating the capability of Fe SAN-PDA@HA to catalyze oxygen production and mitigate hypoxia. Furthermore, the utilization of the H_2O_2 probe (DCF) enabled us to observe the shifts in intracellular H_2O_2 levels after treatment with Fe SAN-PDA@HA. As depicted in Fig. 6f and 6g, the green fluorescence intensity of the Fe SAN-PDA@HA + 808 nm group was markedly lower than that of the control group, signifying the depletion of intracellular H_2O_2, aligning with the experimental outcomes derived from the oxygen probe RDPP. This underscores the exceptional oxygen production proficiency of Fe SAN-PDA@HA within the cellular environment.

To further explore the origin of ROS, the fluorescent probe 2', 7'-dichlorofluorescein diacetate (DCFH-DA) was utilized to detect ·OH radicals in the cells. The results depicted in Fig. 6h revealed intense green fluorescence exclusively in the Fe SAN-PDA@HA group, confirming the production of ROS by Fe SAN-PDA@HA. Moreover, the GSH assay kit was employed to examine the GSH depletion in cells triggered by this composite (Fig. 6j). In comparison to the control group, a notable decrease in intracellular GSH levels was observed in HepG2 cells treated with Fe SAN-PDA@HA composite, indicating the utilization of GSH by Fe SAN-PDA@HA in the cells. Based on the outcomes of the aforementioned experiments, it can be inferred that Fe SAN-PDA@HA with POD mimic activity activity stimulated the production of harmful toxic ROS and depleted GSH in HepG2 cells.

Various experimental groups were subjected to staining with calcein acetoxymethyl/propidium iodide (calcein-AM/PI) to differentiate between live and dead cells. Analysis of the results, as shown Fig. 6i, revealed that cells treated with the control and laser groups displayed green fluorescence, indicating minimal cell damage in these conditions. Conversely, cells in the Fe SAN-PDA@DOX@HA + 808 nm

group emitted a stronger red fluorescence compared to the Fe SAN-PDA@DOX@HA group, suggesting a more pronounced cell-killing effect of laser irradiation and highlighting the critical role of the photothermal properties of the nanomaterial in cell ablation. This observation aligns with the findings from cytotoxicity assessments. The study further delved into quantitatively evaluating apoptosis and necrosis induced by laser-irradiated Fe SAN-PDA@DOX@HA through flow cytometry using double-stained cells with VFITC and 7-aminoactinomycin D (7-AAD). By comparing experimental groups with or without DOX, the interference from DOX was effectively mitigated. The results indicated higher levels of early apoptosis (Q3) and late apoptosis (Q2) indicate a higher number of cell deaths and allow a more thorough evaluation of the therapeutic effect. In the absence of DOX, the combination of Fe SAN-PDA@HA and 808 nm led to an apoptotic ratio of 56% (sum of Q2 + Q3), which was significantly higher compared to Fe SAN-PDA@HA (46.1%) and 808 nm (39.1%) alone (Fig. 6k). Furthermore, the Fe SAN-PDA@DOX@HA + 808 nm group (37.05%) showed increased apoptosis compared to the Fe SAN-PDA@DOX@HA group (31.78%) in the presence of DOX (Figure S24). These results highlight the synergistic cell toxicity resulting from Fe SAN-PDA@HA, drug, and 808 nm laser irradiation, impacting both early and late apoptosis stages.

The effective cell apoptosis induced by Fe SAN-PDA@DOX@HA can be attributed to the combined therapy of CDT, PTT, and CT. The higher level of ·OH radicals and reduced GSH from CDT, effective PTT from Fe SAN-PDA, and CT of DOX all contribute to the promising results seen in tumor treatment. The ability of Fe SAN-PDA@DOX@HA to produce abundant O_2 and ·OH in the TME alleviate tumor hypoxia, enhances the efficacy of DOX chemotherapy, and depletes GSH to increase oxidative stress, ultimately leading to successful eradication of tumor cells. This comprehensive approach shows great potential for improving cancer treatment outcomes.

Antitumor Efficiency Evaluation in Vivo

The therapeutic performance was further evaluated in 4T1 tumor-bearing mice, focusing on the combined CDT/CT/PTT treatment with SAN-PDA@DOX@HA (Fig. 7a). Mice were administered intravenous injections of 5 mg kg^{-1} intravenously for a total of five treatments. Following 10 minutes of 808 nm laser irradiation, mice treated with Fe SAN-PDA@DOX@HA + 808 nm group exhibited a rapid and significant increase in tumor site temperature, reaching 57.1°C (Fig. 7b). In contrast, the control group showed minimal temperature elevation, indicating the safety of laser irradiation for normal tissues. These results suggest effective accumulation of Fe SAN-PDA@DOX@HA nanocomposites at the tumor site, enhancing PTT efficiency. Mice in the treatment groups with DOX + Laser, Fe SAN-PDA@DOX@HA and Fe SAN-PDA@DOX@HA + 808 nm did no display significant differences in body weight over the treatment period, indicating minimal side effects (Fig. 7c). Tumor volume analysis revealed varying degrees of tumor growth inhibition in different treatment groups, as shown in Fig. 7d, with Fe SAN-PDA@HA + 808 nm group demonstrating superior efficacy. The combination of Fe SAN-PDA@HA and DOX exhibited synergistic effects in tumor suppression. These findings underscore the synergistic therapeutic impact of nanozyme catalysis therapy, PTT, and CT. Analysis of post-treatment tumor morphology further confirmed the efficacy of the treatments (Fig. 7e).

The study assessed the iron (Fe) content in major organs and tumors of mice using ICP-OES, while also investigating the metabolic behavior of Fe SAN-PDA@DOX@HA in vivo. Results illustrated in Fig. 7g and S25 revealed that Fe SAN-PDA@DOX@HA primarily accumulated in the spleen after 4 h injection. However, Subsequently, a gradual decrease in Fe content over time indicated the biosafety of Fe SAN-PDA@DOX@HA. Notably, mice treated with DOX + 808 nm or Fe SAN-PDA@DOX@HA + 808 nm exhibited significantly elevated the levels of the inflammatory cytokines (TNF-α) compared to other groups (Fig. 7f), suggesting a robust immune response in mice. Hematoxylin-eosin (H&E) staining on tumors and vital organs reflected significant cell damage in cancer tissues of the Fe SAN-PDA@DOX@HA + 808 nm group, with a larger area of dead cells compared to the Fe SAN-PDA@DOX@HA group. Minimal tissue damage was observed in other major organs (Fig. 7h), indicating that low cardiotoxicity, hepatotoxicity, splenic toxicity, pulmonary toxicity, and renal toxicity of Fe SAN-PDA@DOX@HA on organs. These findings support the favorable biosafety profile of Fe SAN-PDA@DOX@HA and sits potential application in nanozyme catalytic therapy, PTT, and CT tumor triple therapy.

Discussion

In summary, we have proposed a pioneering approach to surface engineering Fe single atom nanozymes with PDA to induce the produce Fe SAN-PDA with multi-mimetic activities tailored for tumor-specific treatment. Notably, presence of abundant quinone structures on the PDA surface facilitates the efficient immobilization of the therapeutic drug DOX through Michael addition/Schiff base reaction. The highly dispersed atomic sites and iron-nitrogen coordination structure of Fe SAN-PDA result in exceptional catalytic performance in TME, demonstrating CAT-like, POD-like, and GPx-like activities. This enables the catalysis of abundant oxygen generation from endogenous H_2O_2, alleviating tumor hypoxia and producing hydroxyl radicals as active oxygen therapeutics, while depleting GSH to modulate intracellular oxidative stress. Remarkably, under 808 nm laser irradiation, Fe SAN-PDA exhibits a notable photothermal conversion efficiency of 53.4%. The Fe SAN-PDA@DOX@HA nanoplatform ensures biocompatibility and integrates nanozyme catalytic therapy, photothermal therapy, and chemotherapy to combat malignant tumors, thereby enhancing tumor treatment efficiency. After intravenous injection of Fe SAN-PDA@DOX@HA followed by 808 nm irradiation, it exhibits potent anti-tumor efficacy with minimal side effects. The innovative strategy for doxorubicin immobilization inspired by the polydopamine engineering not only enables effective regulation of H_2O_2/O_2/GSH and reshaping of the TME but also achieves synergistic CDT/PTT/CT multimodal therapy. The novel immobilization method for DOX loading, coupled with the high loading capacity of the designed single atom nanozyme and the controlled release mechanism, contributes to the significantly enhanced anti-tumor effects in vivo. This strategy of combining multimimetic iron single-atom nanozyme to modulate cellular reactive oxygen and reactive sulfur species with chemotherapy drugs may pave the new approach for nanozyme-mediated synergistic multimodal tumor therapy.

Methods

Materials

Iron (III) 2,4-pentanedionate ($Fe(acac)_3$) (98%, Shanghai Maclean Biochemical Technology Co., LTD), zinc nitrate ($Zn(NO_3)_2$, 99%, Tianjin Kemiou Chemical Reagent Co., LTD), 2-methylimidazole (2-MI, 98%, Sinopharm Chemical Reagent Co. LTD), 3,3',5,5'-tetramethylbenzidine (TMB, 98%, Shanghai Macklin Biochemical Co. LTD., China), dopamine hydrochloride ($C_8H_{11}NO_2 \cdot HCl$, 98%, Aladdin), adriamycin (DOX), hyaluronic acid (HA, 97%, Rhawn), 5,5'-Dithiobis-(2-nitrobenzoic acid) (DTNB, 98%, Shanghai Macklin Biochemical Co. LTD., China), methylene blue trihydrate (MB, Shanghai Macklin Biochemical Co. LTD., China), titanic sulfate ($Ti(SO_4)_2$, 96%, Shanghai Macklin Biochemical Co. LTD., China), coumarin (99.82%, Bide Pharmaceutical Technology Co., Ltd) were used as obtained. Tris(4,7-diphenyl-1,10-phenanthroline) ruthenium(II) dichloride ($Ru(dpp)_3Cl_2$, RDPP) (98%) was purchased from Shanghai Kaiwei Chemical Technology Co., Ltd. 2',7'-Dichlorofluorescein (DCF, 98%) was purchased from Shanghai Maclean Biochemical Technology Co., Ltd. The 2',7'-Dichlorodihydrofluorescein diacetate (H2DCFDA, 99.8%) was purchased from MedChemExpress (Shanghai). Nicotinamide adenine dinucleotide phosphate (NADPH) and glutathione reductase (GR, 1 unit) were obtained from Sigma-Aldrich. Dulbecco's modified Eagle's medium (DMEM) and 1640 medium fetal bovine serum (FBS, 10%) were obtained from Gibco Life Technologies. Hoechst 33342 dyeing solution (10 $\mu g \cdot mL^{-1}$) and 3-(4,5-dimethyl-2-thiazolyl)-2,5-diphenyl tetrazolium bromide (MTT) were purchased from Beijing Solarbio Science & Technology Co., Ltd. All other reagents were analytical reagents. The aqueous solutions used in the experiments were prepared with ultrapure water (18.25 $M\Omega \cdot cm$, Millipore-Q).

Synthesis of Fe SAN-PDA Nanostructures and Preparation of DOX-Loaded Fe SAN-PDA Nanocomposites

The detailed synthesis process for Fe SAN NPs is described in our previous work[34]. 1 mg Fe SAN was dispersed in 20 mL tris (hydroxymethyl) aminomethane hydrochloride (Tris-HCl, pH 8.5) and 1 mg DA was added during agitation. DA was oxidized and self-polymerized on the Fe SAN surface being exposed to air, and Fe SAN-PDA nanostructures were obtained after stirring of 6 h.

800 µL DOX (1 mg/mL) was added in the Fe SAN-PDA solution (500 µg/mL) under stirring for 24 h in dark. The resulting mixture was centrifuged and washed to remove the unloaded DOX. Then, 200 µL HA solution (1 mg/mL) was added in the Fe SAN-PDA@DOX dispersion, stirring for 6 h, and Fe SAN-PDA@DOX@HA nanocomposites were obtained.

Characterization

Scanning electronic microscopy (SEM) images were obtained by Zeiss Sigma 300. Transmission electron microscopy (TEM) images were obtained from Tecnai G2 F20 (FEI, America). UV – vis spectra were measured on UV-2450 spectrophotometer (Shimadzu, Japan). Fluorescence spectra were performed using F-7100 fluorescence spectrometer (Hitachi, Japan). Fourier transform infrared

spectroscopy (FTIR) and X-ray diffractometer (XRD) spectra were measured on Nexus-870 (Thermo Nicolet, America) and Rigaku 2500 X-ray diffractometer, respectively. X-ray photoelectron spectroscopy (XPS) was measured on K-Alpha 1063 (Thermo Fisher Scientific, British). Portable dissolved oxygen tester (JPBJ-608, Shanghai INESA Scientific Instruments Co., Ltd) was used to determinate the dissolved oxygen. Cell viability was determined with a microbiome plate reader (SpectraMax i3, America Molecular Devices). Confocal laser scanning microscope (CLSM) images were obtained by Leica TCS SP8 (Germany). The photothermal properties were measured by infrared thermal imager (Uni-Trend Technology Co., Ltd, UTi165A) and 808 nm laser (Changchun Leishi Photo-Electric Technology Co., Ltd, MW-GX-808/2000 mV). Flow cytometry was recorded by BD FACSanto (America).

Oxidase-like activities of Fe SAN-PDA

To study the OXD-like activity of the obtained Fe SAN-PDA, 50 μL Fe SAN-PDA (100 μg·mL^{-1}) and 100 μL TMB (1 mM) solution were added into HAc-NaAc solution (pH 3.5) with a total volume of 1 mL. UV − vis spectra were recorded after reaction for 15 min at 35°C. TMB solutions with different concentrations were used to study the steady-state kinetics of the OXD-like activity and the Michaelis − Menten curve was obtained using the absorbance intensity at 652 nm. The V_{max} and K_m values can be calculated with the Michaelis equation: $V = V_{max}[S]/(K_m+[S])$, where V_{max}, V, [S], and K_m were the maximum reaction rate, initial reaction rate, concentration of the substrate, and the Michaelis-Menten constant, respectively.

Peroxidase-like activities of Fe SAN-PDA

The POD-like activity of Fe SAN-PDA was conducted in PBS (pH 5.5) with the addition of 50 μL Fe SAN-PDA (200 μg·mL^{-1}), 100 μL H_2O_2 (10 mM) and 100 μL TMB (0.4 mM) with a total volume of 1 mL. UV-vis spectra were recorded after the reaction for 10 min at 35°C. The steady-state kinetics of the POD-like activity was studied under different concentrations of TMB or H_2O_2, and the Michaelis − Menten curve was obtained using the absorbance at 652 nm.

Evaluation of ·OH generation

100 μL Fe SAN-PDA (100 μg mL^{-1}) were added into 100 μL MB solution (3.25 μg mL^{-1}) with H_2O_2 (0.1 mM) in PBS (pH 6.5), fixing the total volume of 1 mL. The relative absorbance was recorded via UV-vis spectrophotometer at the fixed time interval of 2 min. The UV absorbance of the characteristic peak was measured at 660 nm[35]. Specifically, the generation of ·OH was also confirmed by 7-hydroxycoumarin. Fe SAN-PDA (100 μg mL^{-1}) and 100 μL coumarin solution (5 mM) were prepared with H_2O_2 (0.1 mM) in PBS (pH 6.5) by fixing the volume to 1 mL. The fluorescence intensity of 7-hydroxycoumarin (E_x: 332 nm, E_m: 467 nm) was measured in every 5 min.

Catalase-like activities of Fe SAN-PDA

Fe SAN-PDA (2 μg·mL^{-1}) and H_2O_2 (50 mM) were mixed in PBS (pH 5.5, 6.5, 7.4), and the produced oxygen was recorded by a JPBJ-608 dissolved oxygen meter with bubbles being found. Fe SAN-PDA (20

μg·mL^{-1}), 30 μL RDPP (30 μg·mL^{-1}), and H_2O_2 (10 mM) were mixed with PBS (pH 5.5, 6.5, 7.4) with the total volume of 1 mL. After reaction of 15 min, the fluorescence intensity of RDPP was detected after H_2O_2 being catalyzed by the CAT-like activity of Fe SAN-PDA under different pH. The steady-state kinetics of the CAT-like activity was studied in different concentrations of H_2O_2 under pH of 6.5, and the Michaelis-Menten curve for H_2O_2 was obtianed using the absorbance at 240 nm (A_{240nm}). H_2O_2 (1 mM) and Fe SAN-PDA (20 μg·mL^{-1}) were incubated in PBS (0.01 M, pH 6.5) at 37°C for 15 min. The mixture (900 μL) was added to 100 μL $Ti(SO_4)_2$ solution (3.5 mg/mL) for reaction of 10 min. The UV absorbance intensity of the product (Ti-O_2) was measured at 410 nm[36].

Glutathione peroxidase-like activities of Fe SAN-PDA

Fe SAN-PDA (100 μg·mL^{-1}), H_2O_2 (1 mM), GSH (1 mM), nicotinamide adenine dinucleotide phosphate (NADPH) (0.1 mM), and glutathione reductase (GR, 2 μM) were mixed with PBS (pH 7.4). The volume was adjusted to 1 mL, and the UV spectrum was recorded immediately. Using the GSH detection kit of Beyotime, 5,5'-dithiobis-(2-nitrobenzoic acid) (DTNB) react with the mercaptan group (-SH) in GSH to produce yellow products with the maximum absorption at 412 nm, DTNB was used as the probe to test the GSH consumption. Since GSH is easily oxidized when exposed to light, the experiment was conducted in dark. Specifically, deionized water was used as the control group to determine the GSH content with PBS (pH 6.5) treated with Fe SAN-PDA. Finally, DTNB (4 mg/mL) solution was added to the above solution for reaction. The concentration of GSH is 0.04 mM.

Photothermal effect evaluations in vitro

The photothermal process was monitored using an infrared thermal imager device every 15 s intervals. Photothermal properties were evaluated by introducing Fe SAN-PDA with various concentrations (0-200 μg/mL) into 1 mL centrifuge tubes and exposing them to an 808 nm NIR laser at power density of 1.2 W/cm^2 for 8 min. The temperature variation in the solution (200 μg/mL) were monitored over five cycles of laser on/off irradiation (808 nm, 1.2 W/cm^2, 8 min). Fe SAN-PDA (200 μg mL^{-1}) was added into a 1.0 mL centrifuge tube. The NIR laser (808 nm, 1.2 W cm^{-2}) was applied for 10 min, followed by a cooling period. The temperature was monitored every 30 seconds during the laser heating and cooling processes. The control group was treated with deionized water, and the experiment procedures were similar to the experimental group. The photothermal conversion efficiency η was calculated according to the Roper's theory[37]:

$$\eta = \frac{hs(\Delta T_{max} - \Delta T_{\mathrm{surr}}) - Q_{dis}}{I(1 - 10^{-A_{808nm}})}$$

1

Where T_{max}-T_{surr} is 34.5°C; the Q_{dis} (W) represents the heat loss from light absorbed by the container, which was calculated to be approximately equal to 0 mW. The I (W cm^{-2}) represents incident laser

power density, with a value of 1.2 W cm^{-2}; And A is the absorbance of samples at 808 nm. Using data from Fig. 3G and equations (3) and (4), τ_s was determined to be 236.47 s, and hs can be calculated based on the Eq. (2):

$$\mathrm{hs} = \frac{m_D C_D}{\tau_s}$$

2

where, the m_D (1.0 g) and C_D (4.2 J g^{-1} °C^{-1}) are the mass and heat capacity of the solvent, respectively, and θ stands for an introduced dimensionless driving force temperature.

$$\theta = \frac{T - T_{surr}}{T_{max} - T_{surr}}$$

3

$$t = -\tau_s ln\theta$$

4

Release of DOX from Fe SAN-PDA@DOX@HA

The amount of DOX loaded on the Fe SAN-PDA@DOX@HA NPs was determined by measuring the absorbance at 480 nm using the calibration curve of DOX. The release of DOX from the nanocomposites was investigated in PBS at pH 5.5, 6.5, and 7.4. 5 mg Fe SAN-PDA@DOX@HA nanocomposites were dispersed in 5 mL of PBS, and the mixture was then incubated in an oscillator at 37°C with continuous orbital shaking (50 rpm). The supernatant of the mixed solution was collected to measure the amount of released DOX.

$$\mathrm{LoadingCapacity\ (LC\backslash\%)} = \frac{(C_{before} - C_{after})VM_{DOX}}{m_{\mathrm{FeSAN-PDA}}}$$

5

Cell culture

Free DMEM medium contains 10% FBS and 1% streptomycin and penicillin solution. The cells were cultured in a constant temperature incubator at 37°C, with 5% CO_2 used to harvest human cervical cancer (HepG2) cells. Normal human liver cells (LO2) was harvested using 1640 medium containing 10% FBS and 1% streptomycin and penicillin solution as cell medium at 37°C and 5% CO_2 in the air.

In vitro cellular uptake

HepG2 cells were incubated into six-well culture plates at a density of 5×10^5/well and cultured for 24 h. Subsequently, the cells were then treated with the medium containing Fe SAN-PDA@DOX@HA for 1, 2, 4,

and 6 h, respectively. Following staining with Hoechst 33342, the cells were imaged with using a confocal laser scanning microscope (CLSM; Leica TCS SP8, Germany). A flow cytometer was used for quantitative analysis and other experimental procedures were the same as above[38].

In vitro cytotoxicity

The MTT method was used to evaluate the cytotoxicity of DOX, Fe SAN-PDA@HA, Fe SAN-PDA@DOX@HA and Fe SAN-PDA@DOX@HA + 808 nm. HepG2 and LO2 cells were incubated in the 96-well plates and incubated at 37 ℃ with 5% CO_2 in air for 24 h. A blank medium was added to the outermost layer of the 96-well plates. Different concentrations of DOX, Fe SAN-PDA@HA, Fe SAN-PDA@DOX@HA were administered to six parallel cell groups for 24 h, respectively. Some groups were then exposed to 808 nm laser (1.0 W cm^{-2}) for 5 min. After removing the culture media, fresh media containing 0.5 mg mL^{-1} MTT (100 μL) were added to the plates in the incubator for 4 h. The optical density (OD) of the solution was measured at 570 nm using a microplate reader.

The cells viability was calculated using the following formula:

Cell viability (%) = $(OD_{Treated} - OD_{Blank}) / (OD_{Control} - OD_{Blank}) \times 100\%$

where $OD_{Treated}$ and $OD_{Control}$ are the measured OD values of the cells treated with and without the above materials, respectively. OD_{Blank} is the OD value of the plate blank without cells.

Intracellular ROS production

The total ROS, H_2O_2, ·OH, and O_2 production capacity of Fe SAN-PDA@HA was measured by using DCF, DCFH-DA and $[Ru(DPP)_3]Cl_2$ (RDPP) as fluorescent probe, respectively. HepG2 cells were incubated at 37 ℃and 5% CO_2 for 24 h, then culture medium was replaced with 1 mL Fe SAN-PDA@HA (25 μg mL^{-1}) and incubated for 5 hours. After irradiated with 808 nm NIR laser (1.2 W cm^{-2}) for 6 min and incubated for another 30 min, cells were washed with fresh PBS for three times. Then, 10 μM DCF, 10 μM DCFH-DA, or 10 μM $[Ru(DPP)_3]Cl_2$ (RDPP) were added and incubated for 30 min. The cells in Fe SAN-PDA@HA group was treated following the above procedure without 808 nm NIR irradiation and the untreated cells were served as a control group. Cells were washed with fresh PBS for three times, stained with Hoechst 33342. Finally, cells were observed under CLSM (Leica TCS SP8, Germany) after removing all culture media and replacing it with fresh culture media.

Intracellular GSH level

HepG2 cells were incubated in six-well culture plates for 24 h, followed by the incubation of Fe SAN-PDA@HA for overnight. After that, 808 nm laser irradiation (1.2 W/cm^2) was performed for 6 minutes in laser groups. After another 30 min, the cells were washed three times with PBS, and a GSH and GSSG Assay Kit was used to analyze the intracellular GSH level.

Live/Dead cell staining assay

HepG2 cells were initially placed in the confocal laser dishes and then incubated at 37°C with 5% CO_2 in air for 24 h to ensure adherence. Subsequently, the cells were treated with PBS, DOX, Fe SAN-PDA@HA, Fe SAN-PDA@DOX@HA, Fe SAN-PDA@HA + 808 nm, Fe SAN-PDA@DOX@HA + 808 nm for 5 h, respectively. Following this, all cells were placed in an incubator for an additional 12 h. The culture medium was then removed, and the cells were further incubated with PBS containing 2.0 μM Calcein-AM (λex = 494 nm, λem = 517 nm) for 25 min and 5.0 μM PI (λex = 535 nm, λem = 617 nm) for 5 min. After washing the cells three times with PBS, 1 mL PBS were retained in the laser confocal dishes for imaging of living and dead cells using CLSM. A flow cytometer was used for quantitative analysis, and all other experimental procedures remained consistent with those described above.

Animal modal

Male BALB/c mice (5 weeks old) were purchased from Hunan Lake Jingda Experimental Animal Co., LTD. (Hunan, China). All animal experiments were approved by the Animal Ethics Committee of Hubei University of Science and Technology (approval number: 2023-11-503). Construction of subcutaneous tumor model: 1×10^6 4T1 cells were injected subcutaneously into the armpit of the right upper limb of mice to establish a 4T1 subcutaneous tumor model.

Blood circulation and tissue distributions

4T1 cells (100 μL, 1×10^6 cells) were injected subcutaneously into the right upper limb of BALB/c mice to establish a 4T1 breast cancer mouse model. The next experiment was performed when the tumor volume reached about 100 mm^3. 4T1 breast cancer BALB/c mice were injected with Fe SAN-PDA@HA or Fe SAN-PDA@DOX@HA with Fe concentration of 2.255 mg mL^{-1}. The blood was drawn from the tail of the mice 1, 4, 8, and 24 hours post-injection and the tumors and major organs (heart, liver, spleen, lungs, and kidneys) were removed. The Fe content in tumors and major organs was detected by ICP-OES and the blood biochemical indexes of mice were detected for 24 hours.

Antitumor efficiency evaluation in vivo

4T1 BALB/c mice were randomly divided into 8 groups (5 mice per group). (i) PBS; (ii) PBS + 808 nm; (iii) DOX; (iv) DOX + 808 nm; (v) Fe SAN-PDA@HA; (vi) Fe SAN-PDA@HA + 808 nm; (vii) Fe SAN-PDA@DOX@HA; (viii) Fe SAN-PDA@DOX@HA + 808 nm. The drug was administered intravenously every three days, and after 12 hours of injection, groups ii, iv, vi, and viii were exposed to 808 nm laser (1.0 W cm^{-2}) irradiation for 10 minutes, respectively. In the process of irradiation, the temperature changes were monitored by infrared thermal imager. Tumor volume and body weight were monitored every 2 days on the 15th day of treatment. The long diameter (a mm) and short diameter (b mm) of the subcutaneous tumor were measured every 2 days, the tumor volume (V = 1/2 ab^2 mm^3) was calculated, and the relative tumor volume was calculated as V_t/V_0 (Vt was the tumor volume monitored in time after treatment, V_0 was the initial tumor volume).

The mice were euthanized 15 days after treatment to obtain blood, tumors, and major organs for further experiments. Blood is used for blood routine analysis and blood biochemical analysis. Tumors and organs were immobilized with 4% paraformaldehyde for H&E analysis. Representative images of tumor tissue in each group (n = 3) were also taken. The tumors of different groups were collected and analyzed by enzyme-linked immunosorbent assay (ELISA) to determine tumor necrosis factor (TNF)-α.

Photothermal imaging

4T1 cells were injected subcutaneously into the right lower limb for in vivo photothermal imaging. When the tumor grew to about 100 mm^3, 100 μL normal saline or Fe SAN-PDA@DOX@HA (5 mg kg^{-1}) was injected into the tumor. The tumor was irradiated with an 808 nm laser (1.2 W cm^{-2}, 10 min), and the temperature and thermal images of the mouse tumor were measured and recorded with an infrared imager at intervals of 0 min to 8 min.

Statistical analysis

All data are expressed as mean ± standard deviation (SD). The statistical significance of the differences between groups was determined by one-way analysis of variance (ANOVA), followed by the Tukey multiple comparison test. Results Using GraphPad Prism 9.5 software, single factor analysis of variance was used to evaluate the differences between groups. $p < 0.05$(*$p < 0.05$, **$p < 0.01$, ***<0.01, ***<0.001, ***<0.001, ns: not significant)

Declarations

Reporting summary

Further information on research design is available in the Nature Portfolio Reporting Summary linked to this article.

Data availability

All data are available within the Article and Supplementary Files (Supplementary Information, Supplementary Data 1), or available from the corresponding authors upon request. Source data are provided with this paper.

Acknowledgment

This work was financially supported by the National Natural Science Foundation of China (22274047, 21974042, 22274048), the Scientific Research Fund of Hunan Provincial Education Department (18A010), the Science and Technology Department of Hunan Province (2021JJ30012), the Hubei Science and Technology Program (2022CFB781), Innovation Team of Hubei University of Science and Technology (2023T13).

References

1. Chen 1 (2023) Atomic-level regulation of cobalt single-atom nanozymes: engineering high-efficiency catalase mimics. Angew Chem Int Ed 135:e202301879
2. Wang M et al (2023) Defect-induced electron redistribution between Pt-N_3S_1 single atomic sites and Pt clusters for synergistic electrocatalytic hydrogen production with ultra-high mass activity. Adv Funct Mater 34:2309474
3. Sun X et al (2023) Nanozymes with osteochondral regenerative effects: an overview of mechanisms and recentapplications. Adv Healthc Mater 13:2301924
4. Liu Z et al (2022) Genetically engineered protein corona-based cascade nanozymes for enhanced tumor therapy. Adv Funct Mater 32:2208513
5. Liu L et al (2023) Smart nanosensitizers for activatable sono-photodynamic immunotherapy of tumors by redox-controlled disassembly. Angew Chem Int Ed 62:e202217055
6. Xia H et al (2023) Boosting oxygen reduction reaction kinetics by designing rich vacancy coupling pentagons in the defective carbon. J Am Chem Soc 145:25695–25704
7. Li D et al (2023) Spark PtMnIr nanozymes for electrodynamic-boosted multienzymatic tumor immunotherapy. Adv Mater 36:2308747
8. Han Y et al (2023) Modulating the coordination environment of carbon-dot-supported Fe single-atom nanozymes for enhanced tumor therapy. Small 20:2306656
9. Liu Y et al (2023) Multi-enzyme Co-expressed nanomedicine for anti-metastasis tumor therapy by up-regulating cellular oxidative stress and depleting cholesterol. Adv Mater 36:e2307752
10. Zhang Q et al (2024) Injectable hydrogel with doxorubicin-loaded ZIF-8 nanoparticles for tumor postoperative treatments and wound repair. Sci Rep 14:9983
11. Zhu B et al (2023) A glutathione peroxidase-mimicking nanozyme precisely alleviates reactive oxygen Species and promotes periodontal bone regeneration. Adv Healthc Mater 13:2302485
12. Mon M et al (2020) Hydrolase-like catalysis and structural resolution of natural products by a metal-organic framework. Nat Commun 11:3080
13. Huang Y et al (2024) Nanotechnology's frontier in combatting infectious and inflammatory diseases: prevention and treatment. Signal Transduct Target Ther 9:34
14. Zhu Y et al (2023) Photothermal enhanced and tumor microenvironment responsive nanozyme for amplified cascade enzyme catalytic therapy. Adv Healthc Mater 12:2202198
15. Zhu J et al (2023) PtMo-Au metalloenzymes regulated tumor microenvironment for enhanced sonodynamic/chemodynamic/starvation synergistic therapy. Small 19:2303365
16. Wilson WR, Hay MP (2011) Targeting hypoxia in cancer therapy. Nat Rev Cancer 11:393–410
17. Xia H et al (2022) Identifying luminol electrochemiluminescence at the cathode via single-atom catalysts tuned oxygen reduction reaction. J Am Chem Soc 144:7741–7749
18. Tao L et al (2023) Precise synthetic control of exclusive ligand effect boosts oxygen reduction catalysis. Nat Commun 14:6893

19. Wu L et al (2023) Smart lipid nanoparticle that remodels tumor microenvironment for activatable H_2S gas and photodynamic immunotherapy. J Am Chem Soc 145:27838–27849
20. Zhong S et al (2023) Self-driven electricity modulates d-band electrons of copper single-atom nanozyme for boosting cancer therapy. Adv Funct Mater 33:2305625
21. Wang Y et al (2023) Highly active single-atom nanozymes with high-loading iridium for sensitive detection of pesticides. Anal Chem 95:11960–11968
22. Liu Y, Yao M, Han W, Zhang H, Zhang S (2021) Construction of a single-atom nanozyme for enhanced chemodynamic therapy and chemotherapy. Chemistry 27:13418–13425
23. Chen Q et al (2023) Single atom-doped nanosonosensitizers for mutually optimized sono/chemo-nanodynamic therapy of triple negative breast cancer. Adv Sci 10:e2206244
24. Cai S et al (2022) Tumor-microenvironment-responsive cascade reactions by a cobalt-single-atom nanozyme for synergistic nanocatalytic chemotherapy. Angew Chem Int Ed 61:e202204502
25. Liu X et al (2024) A cardiac-targeted nanozyme interrupts the inflammation-free radical cycle in myocardial infarction. Adv Mater 36:e2308477
26. Lee H, Dellatore SM, Miller WM, Messersmith PB (2007) Mussel-inspired surface chemistry for multifunctional coatings. Science 318:426–430
27. Qi P et al (2022) A platelet-mimicking single-atom nanozyme for mitochondrial damage-mediated mild-temperature photothermal therapy. ACS Appl Mater Interfaces 14:19081–19090
28. Farzad E, Veisi H (2018) Fe_3O_4/SiO_2 nanoparticles coated with polydopamine as a novel magnetite reductant and stabilizer sorbent for palladium ions: Synthetic application of Fe_3O_4/SiO_2@PDA/Pd for reduction of 4-nitrophenol and Suzuki reactions. J Ind Eng Chem 60:114–124
29. He S, Feng Y, Sun Q, Xu Z, Zhang W (2022) Charge-switchable Cu_xO nanozyme with peroxidase and near-infrared light enhanced photothermal activity for wound antibacterial application. ACS Appl Mater Interfaces 14:25042–25049
30. Li H et al (2022) Enhanced photothermal effect of functionalized HMPDA@AuNPs microcapsules for near-infrared theranostic treatment of tumor. J Mater Sci 57:7694–7705
31. Deng H et al (2021) Phase-change composites composed of silicone rubber and Pa@SiO_2@PDA double-shelled microcapsules with low leakage rate and improved mechanical strength. ACS Appl Mater Interfaces 13:39394–39403
32. Zeng R et al (2024) Precise tuning of the d-band center of dual-atomic enzymes for catalytic therapy. J Am Chem Soc 146:10023–10031
33. Zhen W, Liu Y, An S, Jiang X (2023) Glutathione-induced in situ michael addition between nanoparticles for pyroptosis and immunotherapy. Angew Chem Int Ed 62:e202301866
34. Liu J et al (2023) Fe-single-atom nanozyme catalysts for sensitive and selective detection of nitrite via colorimetry and test strips. Acs Appl Nano Mater 6:5879–5888
35. Liu J et al (2023) Design and mechanism insight of monodispersed AuCuPt alloy nanozyme with antitumor activity. ACS Nano 17:20402–20423

36. Zhu Y et al (2023) Enhancing catalytic activity of a nickel single atom enzyme by polynary heteroatom doping for ferroptosis-based tumor therapy. ACS Nano 17:3064–3076
37. Chang M et al (2022) Cu single atom nanozyme based high-efficiency mild photothermal therapy through cellular metabolic regulation. Angew Chem Int Ed 61:e202209245
38. Liu F et al (2019) A tumor-microenvironment-activated nanozyme-mediated theranostic nanoreactor for imaging-guided combined tumor therapy. Adv Mater 31:1902885

Schemes

Scheme 1 is available in the Supplementary Files section

Figures

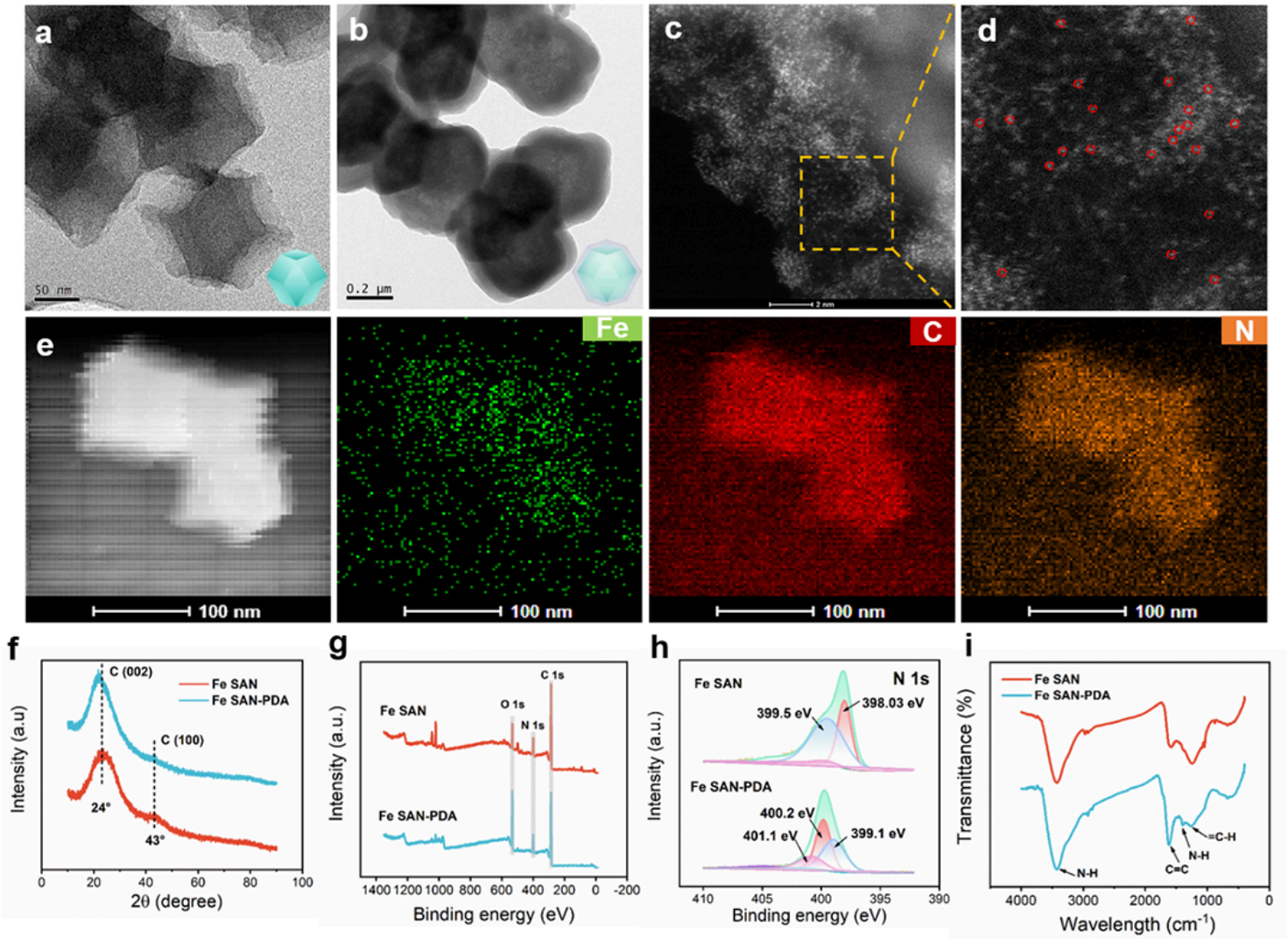


Figure 1

a-b) TEM images of Fe SAN and Fe SAN-PDA. c) Aberration-corrected HAADF-STEM, and d) enlarged images of Fe SAN. Single Fe atoms highlighted by red circles. e) EDS mapping of Fe, C and N elements.

f) XRD pattern of Fe SAN and Fe SAN-PDA. g) XPS survey spectra of Fe SAN and Fe SAN-PDA. h) N1s XPS spectra of Fe SAN and Fe SAN-PDA. i) Fourier transform infrared (FTIR) spectra of Fe SAN and Fe SAN-PDA.

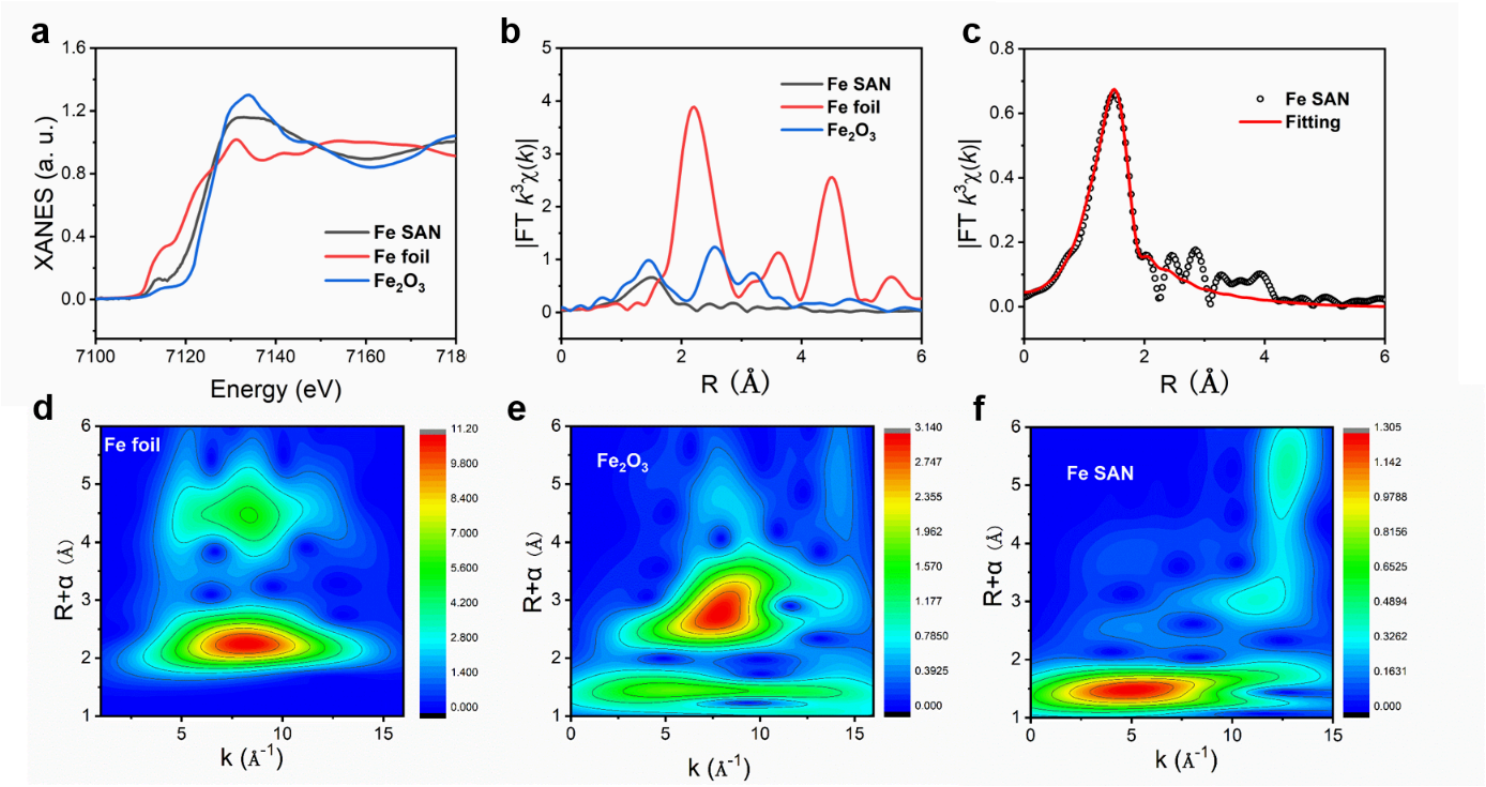


Figure 2

Structural characterization of Fe SAN. a) XANES spectra and b) Fourier transform (FT) extended X-ray absorption fine structure (EXANES) of the Fe K-edge of Fe foil, Fe_2O_3, and Fe SAN. c) Corresponding EXAFS fitting curves of Fe SAN at R space. Wavelet transform (WT) of the samples d) Fe foil, e) Fe_2O_3, f) Fe SAN.

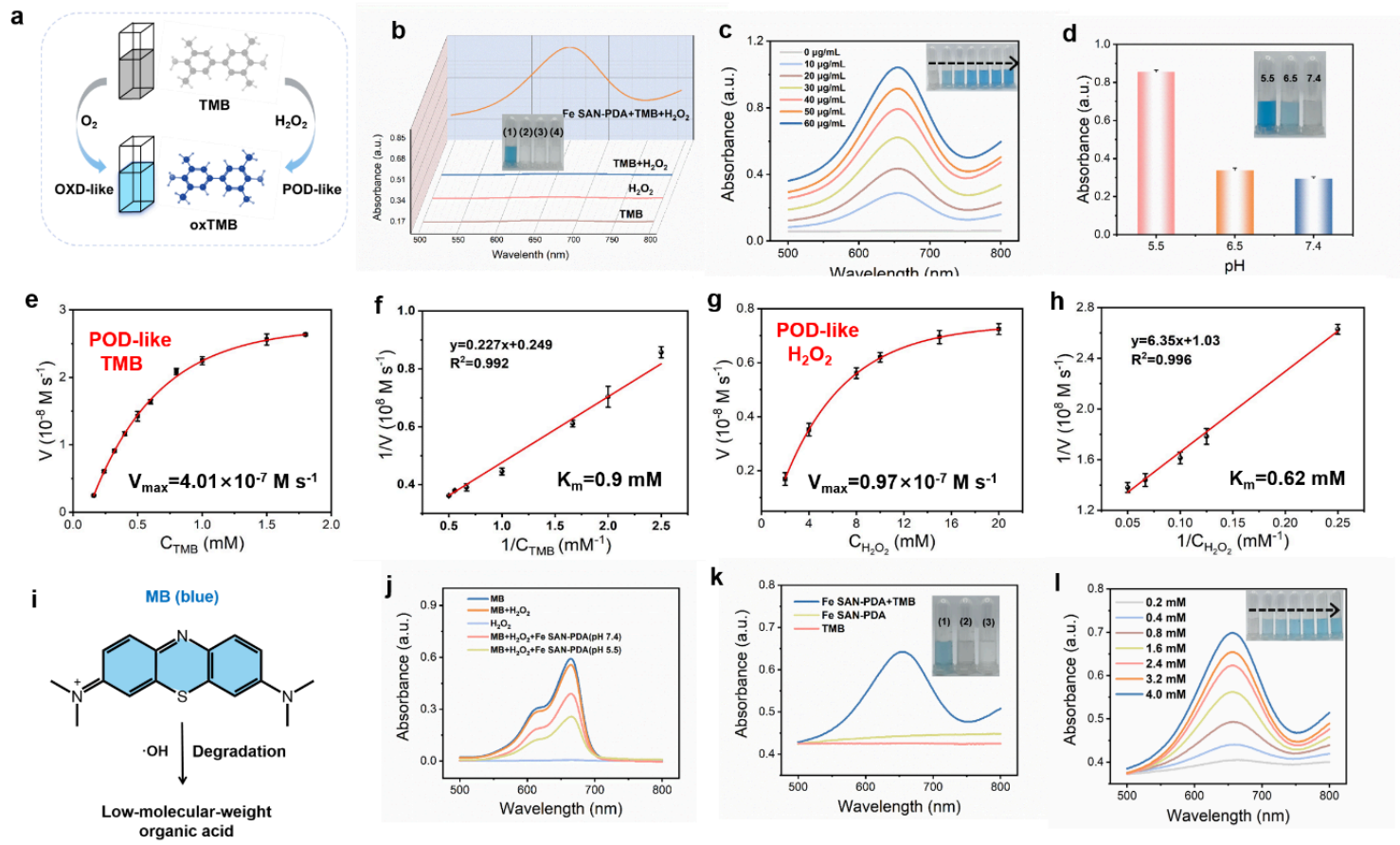


Figure 3

a) Schematic illustration of OXD and POD enzymatic activities of Fe SAN-PDA. b) POD-like activity of the Fe SAN-PDA confirmed with the UV-vis spectra of TMB (pH 5.5, 0.4 mM TMB, 10 mM H_2O_2): (1) Fe SAN-PDA +TMB+ H_2O_2, (2) TMB+ H_2O_2, (3) TMB, (4) H_2O_2. c) The UV spectra of TMB in the presence of Fe SAN-PDA nanomaterials with various concentrations. d) The UV spectra of TMB at various pH (5.5, 6.5, 7.4). POD-like activity of e) and f) Steady-state kinetic assay of the Fe SAN-PDA by using TMB as the substrate. 25 μg·mL^{-1} Fe SAN-PDA, pH 5.5, 10 mM H_2O_2. POD-like activity of g) and h) Steady-state kinetic assay of the Fe SAN-PDA by using H_2O_2 as the substrate. 25 μg·mL^{-1} Fe SAN-PDA, pH 5.5, 0.4 mM TMB. i) Reaction of MB with ·OH to form the colorless products. j) The degradation of MB under different conditions. k) OXD-like activity of the Fe SAN-PDA confirmed with the UV-vis spectra of TMB (pH 4.0, 0.4 mM TMB: (1) Fe SAN-PDA +TMB, (2) Fe SAN-PDA, (3) TMB. l) The UV spectra TMB with various TMB concentrations.

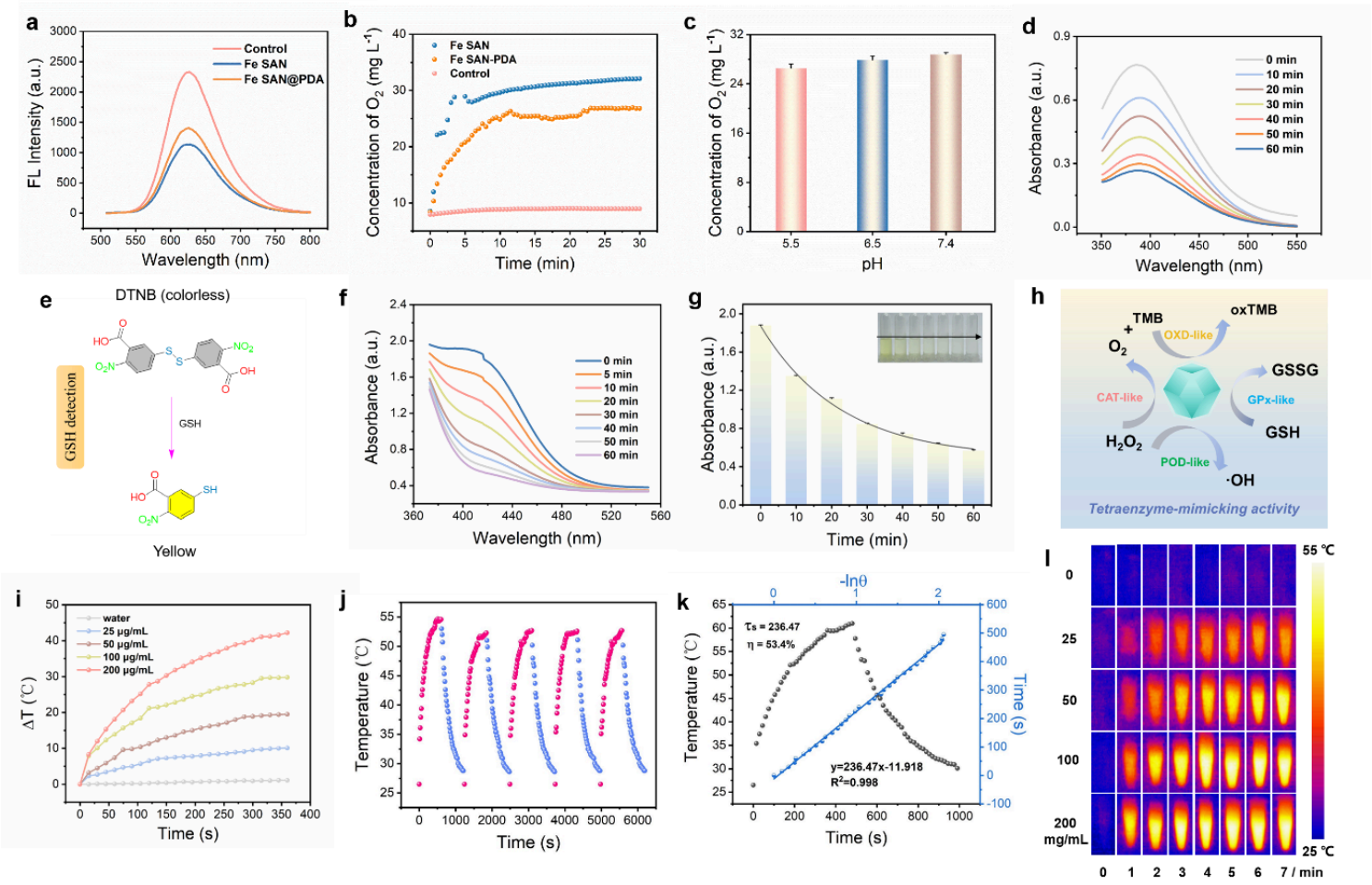


Figure 4

a) Fluorescence spectra of the mixture of H_2O_2, RDPP and Fe SAN/Fe SAN-PDA. 30 μL RDPP (1 mg·mL^{-1}), 200 μL Fe SAN/Fe SAN-PDA (100 μg·mL^{-1}), 200 μL H_2O_2 (10 mM). b) Oxygen generation catalyzed by CAT-like activity of control, Fe SAN and Fe SAN-PDA-mediated catalysis (2.0 μg·mL^{-1}) in PBS (pH 6.5) with 100 mM H_2O_2. c) Oxygen generation catalyzed by CAT-like activity of Fe SAN-PDA for 30 min in PBS with different pH acquiring from dissolved oxygen analyzer. d) The corresponding absorption spectra of H_2O_2-$Ti(SO_4)_2$ solution in the presence of Fe SAN-PDA at different reaction time. e) Reaction principle of colorless DTNB with GSH to produce yellow products. f) and g) Time-dependent GSH consumption with Fe SAN-PDA nanozymes at 100 μg·mL^{-1} Fe SAN-PDA, 0.2 mM DTNB, 200 μM GSH in PBS (pH 7.4). The inset in (g) is the corresponding photograph of the solutions. Data are defined as mean ± S.D. (n=3). h) Schematic illustration of the multi-mimic activity of Fe SAN-PDA to regulate intracellular reactive molecules (GSH/O_2/H_2O_2) in TME. i) Temperature rises and corresponding infrared thermal images of Fe SAN-PDA solutions with various concentrations (0, 25, 50, 100, and 200 μg·mL^{-1}) after irradiation with an 808 nm laser (1.2 W cm^{-2}). j) Photothermal stability of Fe SAN-PDA (200 μg·mL^{-1}) over five cycles of laser on/off under 808 nm laser irradiation. k) Linear time data versus -ln(θ) obtained from the cooling periods of Figure 3j. l) Infrared thermal images of Fe SAN-PDA with different concentration solutions under 808 nm laser irradiation under different time (1.2 W cm^{-2}).

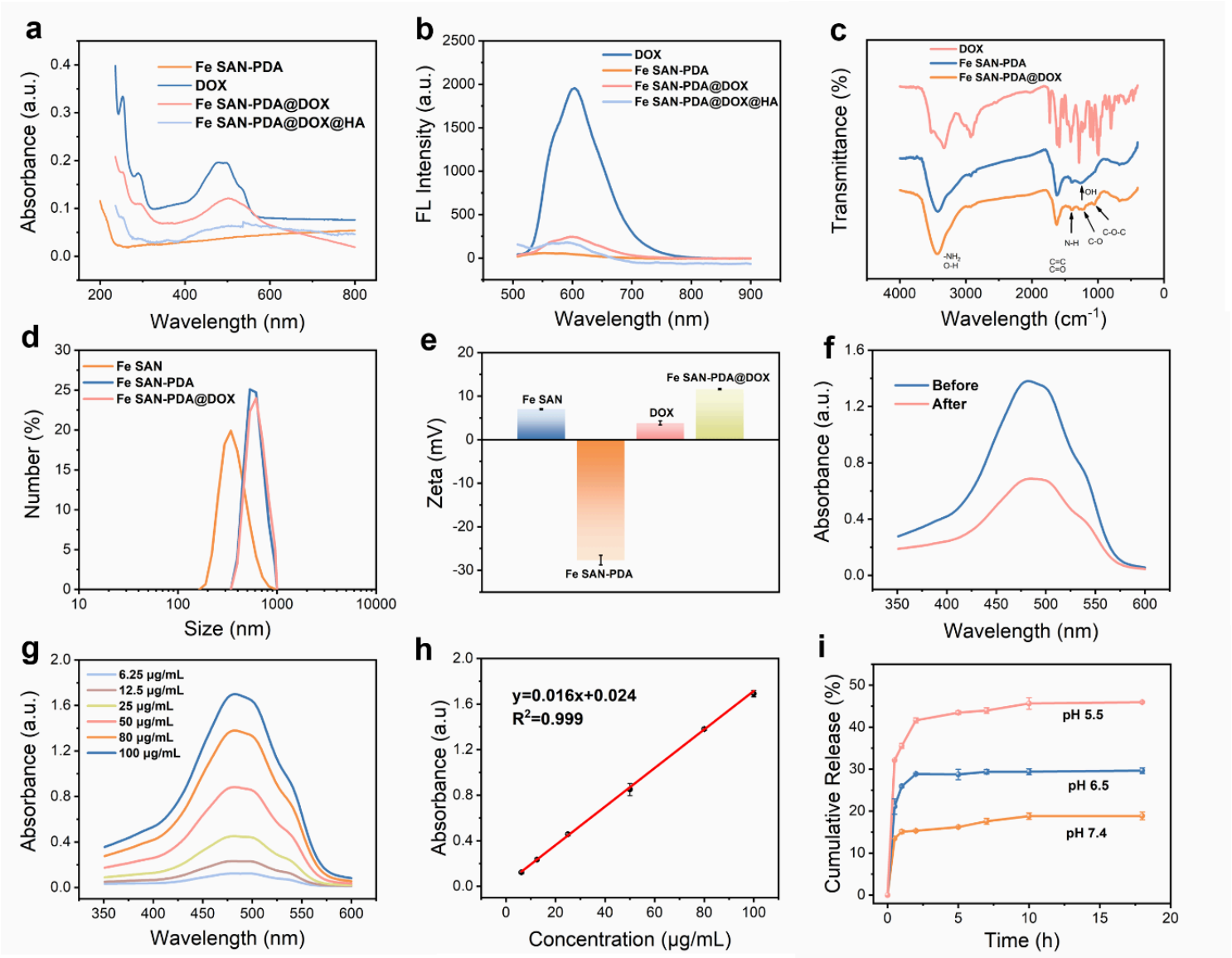


Figure 5

DOX loading/release: a) The UV-Vis spectra and b) Fluorescence spectra of DOX, Fe SAN-PDA, Fe SAN-PDA@DOX and Fe SAN-PDA@DOX@HA. c) FT-IR spectra of DOX, Fe SAN-PDA and Fe SAN-PDA@DOX. d) The variation of the hydrodynamic diameter of Fe SAN, Fe SAN-PDA and Fe SAN-PDA@DOX. e) Zeta potentials of Fe SAN, Fe SAN-PDA, DOX, Fe SAN-PDA@DOX. f) UV-vis spectra of DOX in the supernatant before and after the loading process. g) UV-vis spectra of DOX solution with different concentrations. h) Linear relationship for the absorbance intensity and DOX concentration ranging from 6.25 $\mu g \cdot mL^{-1}$ to 100 $\mu g \cdot mL^{-1}$. i) DOX releasing from Fe SAN@PDA@DOX over time in PBS with different pH.

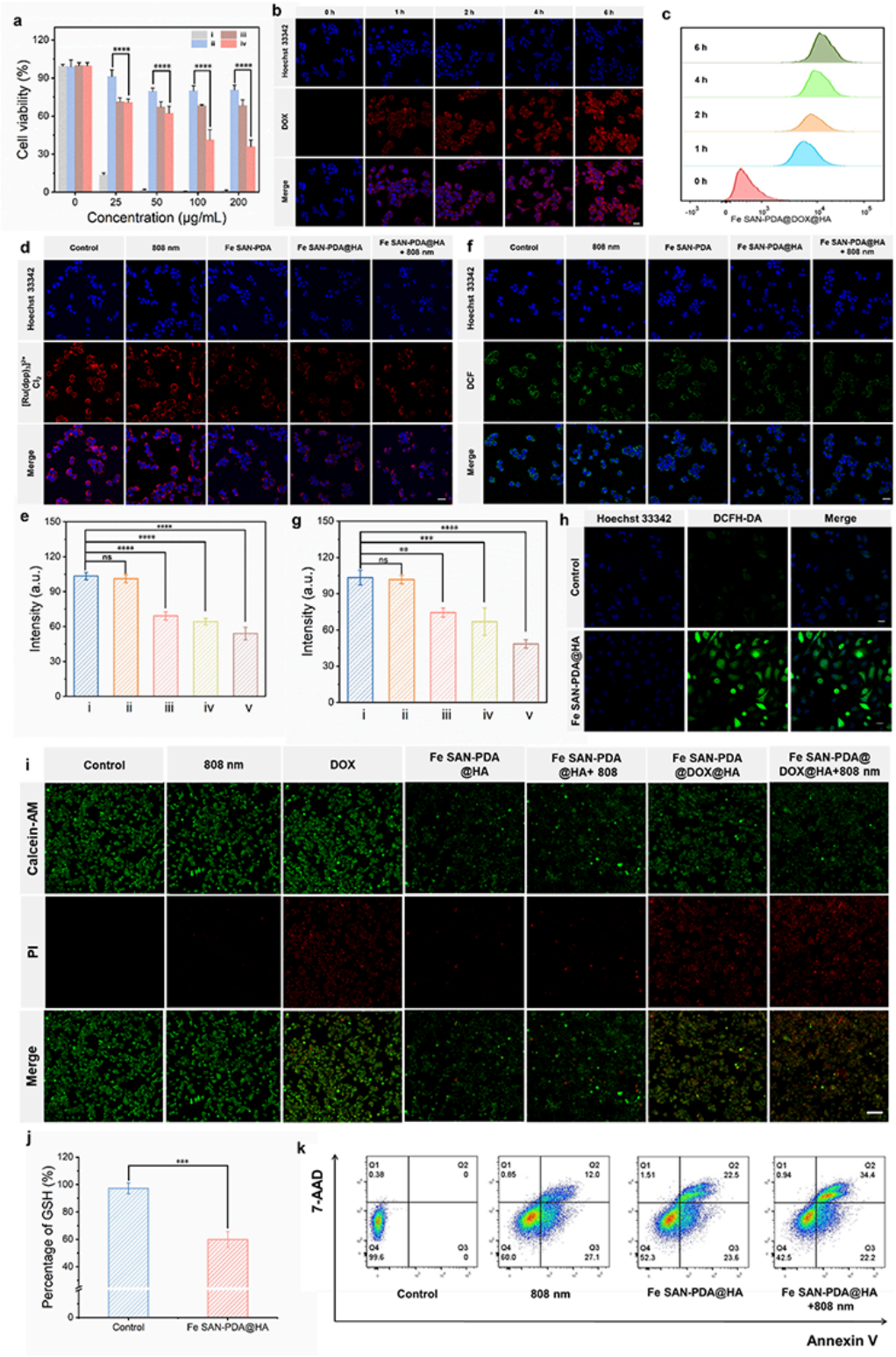


Figure 6

a) Cells viability of HepG2 after incubation with various concentrations of (i) DOX, (ii) Fe SAN-PDA@HA, (iii) Fe SAN-PDA@DOX@HA and (iv) Fe SAN-PDA@DOX@HA+ 808 nm. CLSM images b) and Flow cytometry analysis of DOX c) of HepG2 cells incubation with Fe SAN-PDA@DOX@HA with different incubation time, scale bar: 25 μm. d-f) CLSM images of HepG2 cells using the FL probes for monitoring the intracellular O_2 (d) and H_2O_2 f) levels with different treatment groups. Blue fluorescence of Hoechst

33342, red fluorescence of RDPP hypoxia probe, green fluorescence of the DCF-H_2O_2 probe (scale bar: 25 μm). Corresponding FL intensity of RDPP e) and DCF g) treated with (i) control, (ii) 808 nm, (iii) Fe SAN-PDA, (iv) Fe SAN-PDA@HA, (v) Fe SAN-PDA@HA+808 nm (n=5, scale bar = 25 μm). h) CLSM images of DCFH-DA staining (scale bar: 25 μm). i) CLSM images of HepG2 cells after incubation under various treatments stained with calcein-AM (living cells, green) and PI (dead cells, red). Scale bar: 100 μm. j) Depletion of GSH in tumor cells. k) Flow cytometry analysis of apoptotic HepG2 cells after various treatments using Annexin V-APC/7-AAD staining. The quadrants from the lower left to the upper left (counterclockwise) represent healthy (Q4), early apoptotic (Q3), late apoptotic (Q2), and necrotic cells (Q1). The percentage of cells in each quadrant was shown on the graphs.

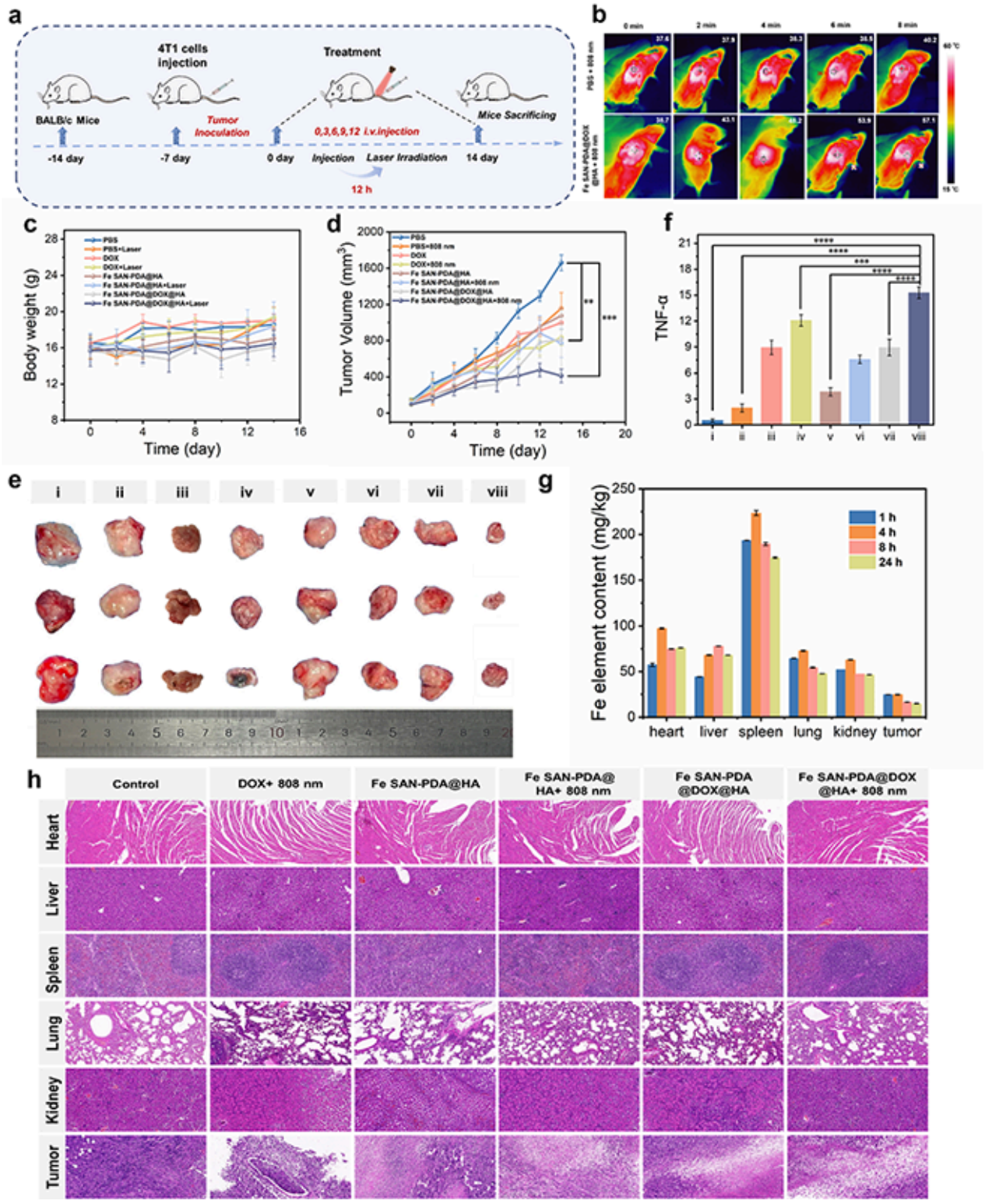


Figure 7

In vivo tumor suppression study. a) Schematic illustration of therapeutic process based on Fe SAN-PDA@DOX@HA. b) Thermal IR images of 4T1 tumor-bearing mice with and without Fe SAN-PDA@DOX@HA injection (5 mg kg^{-1}) exposed to 808 nm laser (1.0 W cm^{-2}, 10 min). c) Time-dependent body weight of the 4T1 tumor-bearing mice and d) Tumor volume curves at different groups (n=3, mean ± SD). e) Photographs of the tumor after different treatment groups on 15 days, (i) PBS; (ii) PBS+808 nm;

(iii) DOX; (iv) DOX+808 nm; (v) Fe SAN-PDA@HA; (vi) Fe SAN-PDA@HA+808 nm; (vii) Fe SAN-PDA@DOX@HA; (viii) Fe SAN-PDA@DOX@HA+808 nm. f) TNF-α level of mice after various treatments. g) Fe element content of different organs for Fe SAN-PDA@DOX@HA by ICP-OES. h) H&E staining of main organs and tumors after different treatments (Scale bar: 100 μm. (*p < 0.05, **p < 0.01, ***p < 0.001, ****p < 0.0001, ns: not significant).

Supplementary Files

This is a list of supplementary files associated with this preprint. Click to download.

- TOC.docx
- SupportingInformation.docx
- Scheme1.png